

Article

Peroxymonosulfate Activation by Photoelectroactive Nanohybrid Filter towards Effective Micropollutant Decontamination

Wenchang Zhao ¹, Yuling Dai ², Wentian Zheng ² and Yanbiao Liu ^{2,*} 

¹ Fujian Provincial Key Laboratory of Featured Materials in Biochemical Industry, College of Chemistry and Materials, Ningde Normal University, Ningde 352100, China; wenchangzhao@foxmail.com

² Textile Pollution Controlling Engineering Center of Ministry of Environmental Protection, College of Environmental Science and Engineering, Donghua University, Shanghai 201620, China; 2202084@mail.dhu.edu.cn (Y.D.); 2191678@mail.dhu.edu.cn (W.Z.)

* Correspondence: yanbiaoliu@dhu.edu.cn; Tel.: +86-21-67798752

Abstract: Herein, we report and demonstrate a photoelectrochemical filtration system that enables the effective decontamination of micropollutants from water. The key to this system was a photoelectric-active nanohybrid filter consisting of a carbon nanotube (CNT) and MIL-101(Fe). Various advanced characterization techniques were employed to obtain detailed information on the microstructure, morphology, and defect states of the nanohybrid filter. The results suggest that both radical and nonradical pathways collectively contributed to the degradation of antibiotic tetracycline, a model refractory micropollutant. The underlying working mechanism was proposed based on solid experimental evidences. This study provides new insights into the effective removal of micropollutants from water by integrating state-of-the-art advanced oxidation and microfiltration techniques.

Keywords: nanohybrid filter; photoelectrochemical filtration; carbon nanotubes; MIL-101(Fe); tetracycline



Citation: Zhao, W.; Dai, Y.; Zheng, W.; Liu, Y. Peroxymonosulfate Activation by Photoelectroactive Nanohybrid Filter towards Effective Micropollutant Decontamination. *Catalysts* **2022**, *12*, 416. <https://doi.org/10.3390/catal12040416>

Academic Editor: Pedro B. Tavares

Received: 15 March 2022

Accepted: 4 April 2022

Published: 7 April 2022

Publisher's Note: MDPI stays neutral with regard to jurisdictional claims in published maps and institutional affiliations.



Copyright: © 2022 by the authors. Licensee MDPI, Basel, Switzerland. This article is an open access article distributed under the terms and conditions of the Creative Commons Attribution (CC BY) license (<https://creativecommons.org/licenses/by/4.0/>).

1. Introduction

Recently, the environmental pollution associated with organic micropollutants in aquatic environments has received increasing environmental concern [1,2]. Micropollutants mainly consist of a vast and expanding category of anthropogenic substances such as pharmaceutical and personal care products (PPCP) and many other emerging compounds [3,4]. Their limited concentration and vast diversity have posed tremendous challenges for current wastewater treatment [5]. It is therefore highly desirable to develop advanced treatment approaches to remove micropollutants from water.

Peroxymonosulfate (PMS)-based advanced oxidation technology has recently emerged as a promising solution to address this issue [6]. Various heterogeneous catalysts have been widely used for PMS activation to produce highly reactive species. Among these, iron-based catalysts are of particular interest due to their exceptional high performance and cost effectiveness [7,8]. Yet, their application is significantly hindered by the challenges associated with the post-separation of powder-like catalysts from the reaction solution, potential Fe ion leaching and poor mass transport in conventional batch reactors. To immobilize the catalysts onto a carbonaceous support could avoid the agglomeration issue of powder-like materials. To this end, carbon nanotubes (CNTs) may serve as the ideal platform to host these nanoscale catalysts because of their rich surface chemistry, excellent electrical conductivity, large surface area and desirable chemical stability [9,10]. We have previously developed a photoelectrochemical filtration system that enables the effective detoxification of toxic heavy metal ions using photogenerated holes (h^+) (e.g., to transform highly toxic Sb(III) into less toxic Sb(V)) [11]. The key to this system was a nanohybrid filter consisting of electroactive CNT and photo-responsive metal-organic frameworks (MOF, MIL-88(B)). These introduced Fe ions were uniformly distributed onto oxylated functional moieties

of CNT, and the exerted electric field favors the cycling of $\text{Fe}^{3+}/\text{Fe}^{2+}$ pairs [12]. This not only avoids the post-separation of the MIL-88(B) catalysts, but also demonstrates enhanced material stability. In addition, the flow-through design outperformed the conventional batch reactor due to convection-enhanced mass transport [13].

Based on these findings, we hypothesized that such photoelectrochemical filtration design may also serve as a high-performance system towards PMS activation and micropollutant decontamination. On one hand, under irradiation, the photogenerated holes (h^+) may directly contribute to the degradation of organic micropollutant molecules upon contact or indirectly induce the generation of other aggressive reactive radicals (such as hydroxyl radicals) [14]. The applied electric field would facilitate the cycling of $\text{Fe}^{3+}/\text{Fe}^{2+}$ within the system [15]. On the other hand, the photogenerated electrons (e^-) may cleave the O–O bond of PMS via the one-electron pathway; also, CNT itself was proven to be effective to activate PMS via nonradical pathway [16,17]. All these routes collectively contribute to the effective degradation of micropollutants in water. To do this, we firstly report on the preparation and demonstration of a MIL-101(Fe)@CNT nanohybrid filter to serve as both an electrode material and a filtration medium. Among them, the MIL-101(Fe) exhibits excellent light absorptive ability and large specific surface area properties, while the conductive CNT network structure promotes the separation of e^- and h^+ . The catalytic degradation performance was tested using antibiotic tetracycline as the model micropollutant. Secondly, the effects of operational parameters and environmental factors on the efficacy of the proposed photoelectrochemical filtration system was systematically investigated. A plausible underlying working mechanism of the technology was proposed based on extensive experimental evidence. The outcomes of the present study are dedicated to providing an enhanced strategy towards the effective decontamination of micropollutants from water.

2. Results and Discussion

2.1. Characterization of the Nanohybrid Filter

Figure 1 compares the FESEM image of the conductive CNT filter in the absence and presence of MIL-101(Fe) nanoparticles. As can be seen, the pristine CNT filter showed a smooth surface with CNT intertwined with it to form a 3D porous network. The introduction of MIL-101(Fe) led to a rather rough surface, and those nanoparticles were uniformly distributed on the CNT surface. Furthermore, as the iron precursor concentration increased from 0 to 3 mM, the loading amount of MIL-101(Fe) gradually increased consequently. However, further increasing the precursor concentration to 4.5 mM leads to evident particle agglomeration. The successful loading of MIL-101(Fe) was further verified by the XRD pattern of the MIL-101(Fe)@CNT nanohybrid filter. The characteristic diffraction peaks centered at 8.5, 9.1, 18.6, 21.4 and 25.0° were observed, in good accordance with that of MIL-101(Fe) [7] (Figure S1a). The TGA curve indicated that approximately 1.1 mg of MIL-101(Fe) was loaded onto an effective filtration area of 7.1 cm² (Figure S1b). In addition, the atomic ratio of C, O and Fe on the composite filter surface was 86.92%, 11.80% and 1.31%, as determined by the energy-dispersive spectra analysis (Figure S2). All this evidence collectively indicated the successful preparation of the MIL-101(Fe)@CNT nanohybrid filter. Since MIL-101(Fe) is a well-known photocatalyst with several intriguing attributes, the cyclic voltammetry curve of the MIL-101(Fe)@CNT nanohybrid filter in 50 mM Na_2SO_4 electrolyte solution was examined (with/without UV light irradiation). The saturated photocurrent intensity was 2.05 times higher than that in the absence of light irradiation, suggesting a significant contribution from MIL-101(Fe) (Figure S3a). Electrochemical impedance spectroscopy analysis showed a charge transport resistance of 141.7 Ω for the MIL-101(Fe)@CNT nanohybrid filter, much lower than that of MIL-101(Fe) (1333.1 Ω , Figure S3b). This indicates that the combination of CNT and MIL-101(Fe) favors the separation of photogenerated electron-hole pairs and the rapid transport of photogenerated electrons throughout the conductive networks [11].

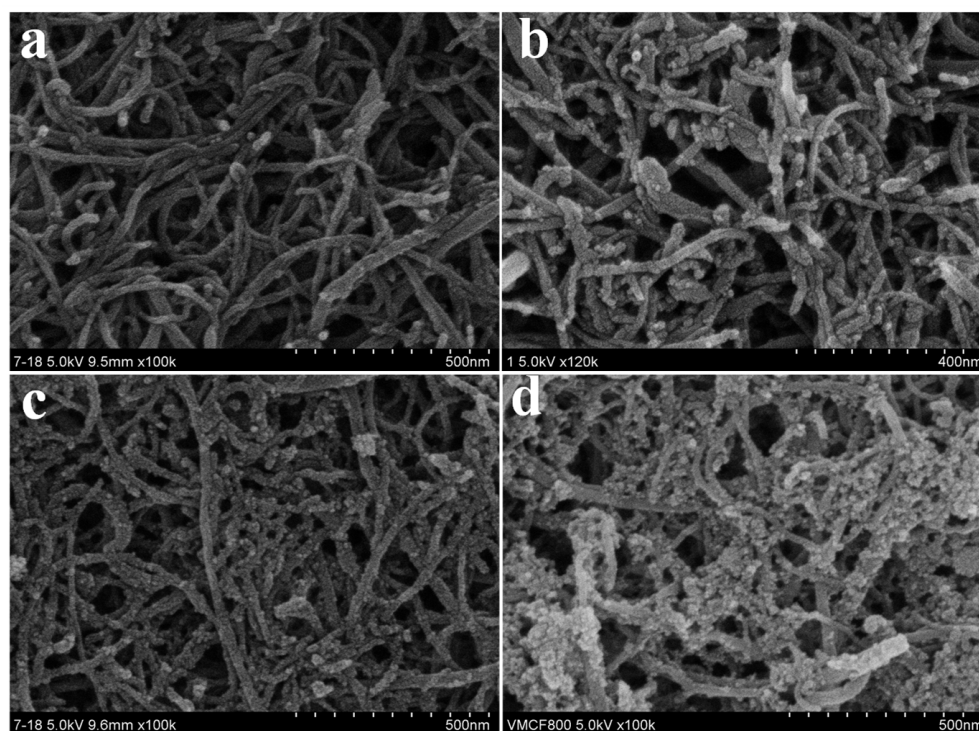


Figure 1. Characterization: comparison of the FESEM image of (a) CNT filter and (b–d) the presence of varying amounts of MIL-101(Fe).

2.2. Photoelectrochemical Degradation of Tetracycline

After successful preparation of the MIL-101(Fe)@CNT nanohybrid filter, we further examined its efficacy towards the photoelectrical activation of PMS to degrade antibiotic tetracycline in a continuous-flow configuration. As shown in Figure 2, only 13.9% TC removal within 20 min was achieved in the presence of PMS alone due to its limited oxidative ability [18].

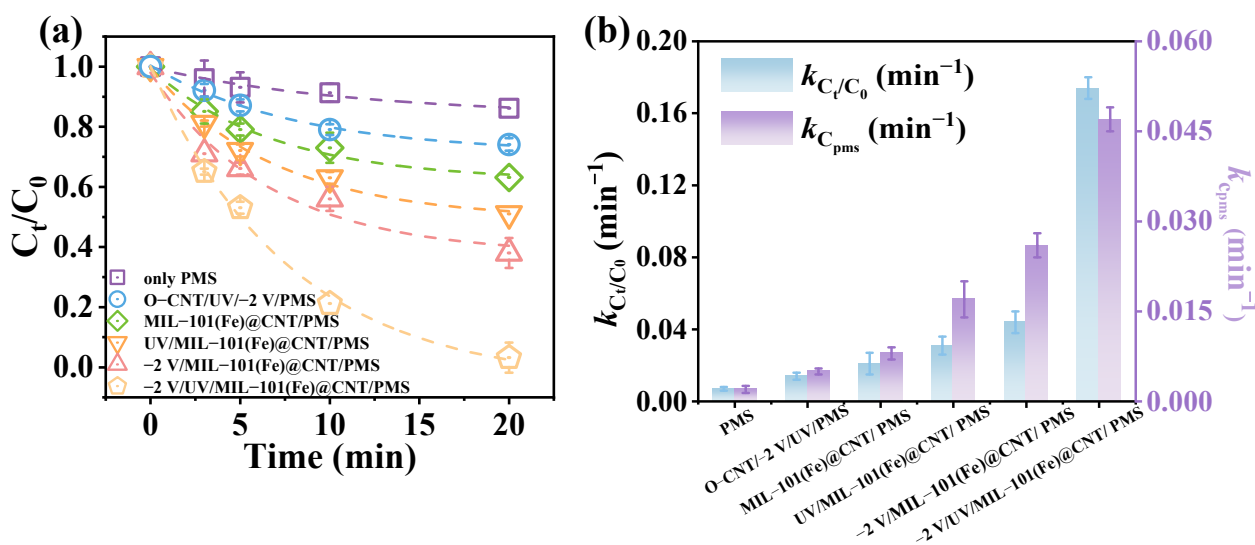


Figure 2. Photoelectrochemical degradation of TC in different systems: (a) TC degradation and (b) corresponding rate constants and rate constants of residual PMS concentrations without TC addition in different systems. Experimental conditions: MIL-101(Fe)@CNT = 3 mM, $[\text{TC}]_0 = 20 \text{ mg L}^{-1}$, applied voltage = -2 V , illumination voltage = 3.8 V , pH = 6.0.

Since the catalytic reaction was conducted after the sorption saturation of the CNT filter, any contributions from physical adsorption of the filter can be excluded. A 25.9% TC removal was observed using a CNT-alone filter when exerting UV irradiation and electric field. This indicates that the PMS activation by UV and electric field is not very effective. Further combining the CNT filter with the MIL-101(Fe) catalyst, i.e., the MIL-101(Fe)@CNT nanohybrid filter, only leads to a TC removal efficiency of 36.8% without applying UV irradiation and electric field, indicating that the catalytic activity of MIL-101(Fe) towards PMS activation is limited as well, possibly due to the short residence time within the filter [19,20]. Moreover, the composite (128.1 mg L⁻¹) has a relatively high specific area compared to CNT (99.6 mg L⁻¹), which can be ascribed to the introduction of MIL-101(Fe) and the formation of a densely covered three-dimensional network. The TC removal efficiency further increased to 49.2% or 62.1%, respectively, by applying UV irradiation or electric field to the MIL-101(Fe)@CNT nanohybrid filter with corresponding pseudo-first-order rate constants (*k*) of 0.031 min⁻¹ and 0.044 min⁻¹ (Table S1). It is of note that an evident photo-electric synergistic effect was identified. When simultaneously applying UV irradiation and electric field, a complete TC removal was obtained using the nanohybrid filter within the same reaction period. The *k* of 0.174 min⁻¹ was 5.6 times and 3.95 times higher than that only applying UV irradiation and electric field, respectively. In addition, PMS self-decomposition rate using the MIL-101(Fe)@CNT nanohybrid filter in different catalytic systems was also determined. As shown in Figure S4, the residual PMS in the photoelectrochemical, photocatalytic, electrocatalytic and PMS-alone systems was 0.35 mM, 0.56 mM, 0.71 mM and 0.85 mM, respectively, with a corresponding decay rate constant of 0.047 min⁻¹, 0.026 min⁻¹, 0.017 min⁻¹ and 0.008 min⁻¹. As a comparison, the residual PMS and decay rate constants using a CNT-alone filter in a photocatalytic system were 0.90 mM and 0.014 min⁻¹, respectively. All these encouraging results quantitatively exemplified the advantages of combining UV irradiation, electric field, MIL-101(Fe) and CNT towards effective cleavage of the O–O bond of PMS and efficient TC removal [21].

2.3. Mechanism Insights

EPR and quenching experiments were conducted to examine the responsible reactive species within the proposed photoelectrochemical filtration system. As shown in Figure 3a and b, in the PMS-alone system, only very weak signals associated with the quartet DMPO–HO• adduct (1:2:2:1) and the triplet TEMP–¹O₂ adduct (1:1:1) were identified [22,23]. This suggests that reactive oxide species (ROS) are hardly generated from the self-decomposition of PMS. In other cases, characteristic peaks of DMPO–HO• and TEMP–¹O₂ adducts were detected, and the strongest signals were obtained in the photoelectrochemical filtration system. The characteristic signals of the DMPO–SO₄•⁻ adduct was only detected in the presence of the MIL-101(Fe)@CNT nanohybrid filter. This phenomenon could be explained by the unique Fe³⁺/Fe²⁺ interconversion property of MIL-101(Fe) [24]. For example, Bi et al. [25] prepared graphitic carbon-nitride-functionalized MIL-101(Fe) that removed 100% of tetracycline hydrochloride within 40 min, which was attributed to the generation of SO₄•⁻ and HO• active species assisted by visible light coupled with the composite.

Furthermore, quenching experiments were further employed to identify the dominant reactive species involved in the photoelectrochemical filtration system. Methanol can selectively quench with both SO₄•⁻ (*k* = 2.5 × 10⁷ M⁻¹ s⁻¹) and HO• (*k* = 9.7 × 10⁸ M⁻¹ s⁻¹), whereas TBA is more selective for HO• (*k* = 3.8 × 10⁸ M⁻¹ s⁻¹) than SO₄•⁻ (*k* = 4.0 × 10⁵ M⁻¹ s⁻¹) and L-histidine was used to quench the ¹O₂ [6,19]. As displayed in Figure 3c, the TC removal efficiency decreased from 100% (*k* = 0.165 min⁻¹) to 46.7% (*k* = 0.028 min⁻¹) with the increase in spiked methanol from 0 to 100 mM (Table S2). Further increasing the methanol concentration failed to further inhibit the TC removal, suggesting a limited amount of the radical species. A similar phenomenon was also observed by spiking L-histidine as the ¹O₂ scavenger (Figure 3d). These observations inferred the collective contribution from both radical and nonradical pathways towards TC removal. Based on the quenching analysis, the specific contribution from SO₄•⁻, HO• and ¹O₂ accounts for 16.6%, 36.7% and 46.7%,

respectively (Figure S5a). In addition, to further confirm the role of $^1\text{O}_2$, the TC degradation experiment was repeated in the deuterated solvent, since the lifetime of $^1\text{O}_2$ in D_2O (20–32 μs) is one order of magnitude longer than that in H_2O (2 μs) [19]. As shown in Figure S5b, at a TC concentration of 40 mg L^{-1} , the degradation efficiency in D_2O (79.2%, $k = 0.071 \text{ min}^{-1}$) was much higher than in H_2O (57.1%, $k = 0.037 \text{ min}^{-1}$), again suggesting that $^1\text{O}_2$ was the dominant reactive species in the proposed system.

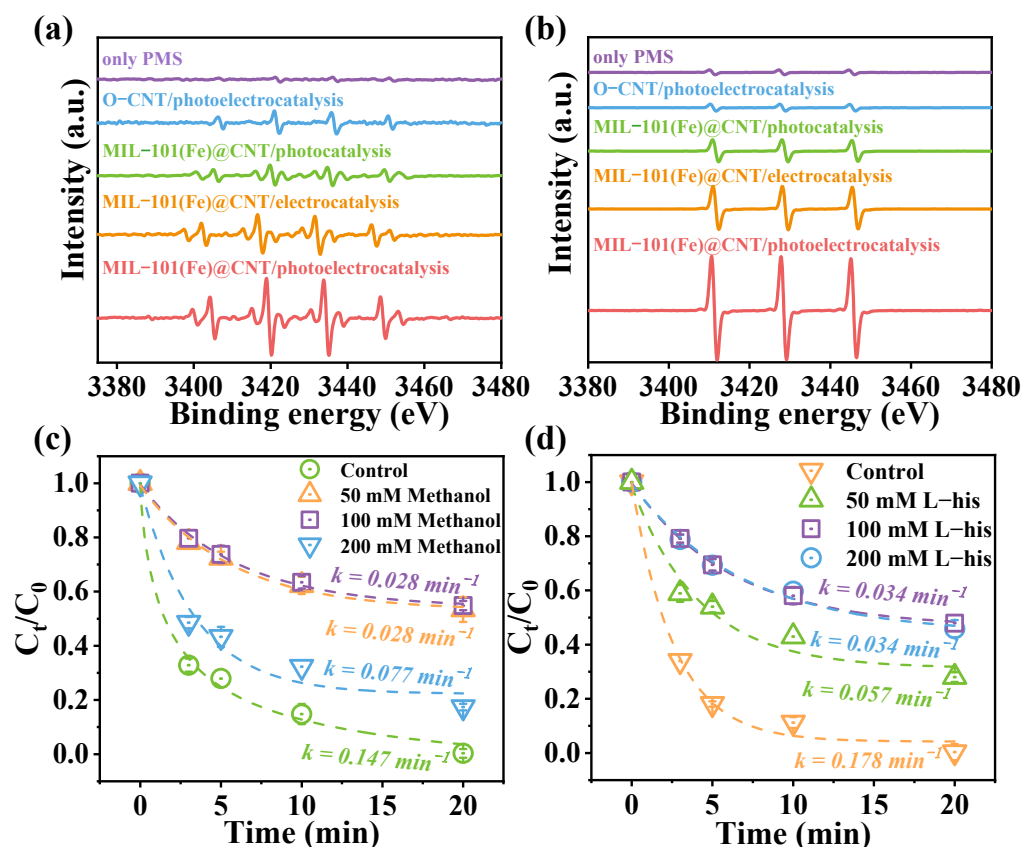
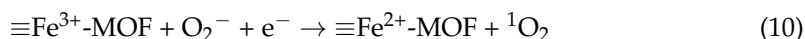


Figure 3. Identification of active species: EPR spectra for the presence of (a) DMPO and (b) TEMP, (c,d) and effect of different capture agents on TC removal. Experimental conditions: MIL-101(Fe)@CNT = 3 mM, $[\text{TC}]_0 = 20 \text{ mg L}^{-1}$, applied voltage = -2 V , illumination voltage = 3.8 V , pH = 6.0.

A plausible working mechanism of the proposed photoelectrical filtration system was proposed as follows: Firstly, under UV irradiation, photogenerated electrons (e^-) and photogenerated holes (h^+) were generated at the solid/liquid interface of the MIL-101(Fe)@CNT nanohybrid filter (Equation (1)) [11]. Thus, Fe^{3+} -MOF reacts with e^- to form Fe^{2+} -MOF (Equation (2)), and the highly aggressive h^+ ($E^0 = 2.67 \text{ V vs. NHE}$) reacts with TC molecules to achieve degradation or reacts with H_2O to generate HO^\bullet ($E^0 = 2.8 \text{ V vs. NHE}$) [11,19]. The applied external electric field facilitates the effective separation of e^- and h^+ and decreases their recombination rate. Meanwhile, PMS can also generate active species with strong oxidation under the action of UV light, such as $\text{SO}_4^{\bullet-}$ ($E^0 = 2.5\text{--}3.1 \text{ V vs. SHE}$) and HO^\bullet (Equation (3)). The applied electric field can not only promote the cycling of $\text{Fe}^{3+}/\text{Fe}^{2+}$, but also promote the decomposition of PMS to generate reactive radicals (Equation (4)) [26,27]. Subsequently, these in situ formed Fe^{2+} species can activate the cleavage of the PMS O–O bond to generate $\text{SO}_4^{\bullet-}$ (Equation (5)). In addition, $\text{SO}_4^{\bullet-}$ can be further transformed into HO^\bullet radicals under certain conditions (Equation (6)) [28] and participate in the oxidative degradation of TC. On the other hand, the nonradical route also plays an essential role in TC degradation. The generation of $^1\text{O}_2$ can either be generated by the reaction of SO_5^- with FeMOF

(Equations (7) and (8)) [22] or by receiving electrons from Fe^{2+} through dissolved O_2 to generate O_2^- and then $^1\text{O}_2$ (Equations (9) and (10)).

Moreover, it has been reported that the carbonyl groups (C=O) of CNT may also facilitate the PMS decomposition to generate $^1\text{O}_2$ [16]. The XPS results (Figure S6a and Table S3) suggest that the C=O content of the nanohybrid filter decreases by 9% after the catalytic reaction, while the C–O content increases by 11%. This indicates that these electron-rich C=O groups may be involved in the cleavage of the PMS O–O bonds by sacrificing electrons. It has been reported that glutaraldehyde surface modification significantly increased the surface density of carbonyl groups on carbon nanotubes and promoted peroxydisulfate generation of $^1\text{O}_2$ [29]. The XPS spectra also suggested a decreased $\text{Fe}^{2+}/\text{Fe}^{3+}$ ratio (by 10%) on a used nanohybrid filter after the photoelectrocatalytic reaction, confirming that the redox conversion of $\text{Fe}^{3+}/\text{Fe}^{2+}$ acts as an electron transfer mediator during the PMS activation process (Figure S6b and Table S4). Finally, the effective TC degradation was further verified by a TOC mineralization of 51.7% over a 20 min reaction (Equation (11)).



2.4. Operational Parameters Optimization

2.4.1. Impacts of MIL-101(Fe) Loading and Applied Voltage

As displayed in Figure 4a, as the precursor concentration increased from 1.5 to 3 mM, the TC degradation efficiency and the corresponding k increased from 68.1% to 97.5% and 0.053 min^{-1} to 0.179 min^{-1} , respectively (Table S5). This suggested that a higher MIL-101(Fe) loading favors the acceleration of the TC degradation kinetics by providing abundant reactive sites for the catalytic reaction. However, further increasing the precursor concentration to 4.5 mM deteriorated the TC removal kinetics, owing to the agglomeration of the as-formed MIL-101(Fe) particles as well as the inevitable burying of the surface-active sites on the nanohybrid filter (Figure 1d) [11]. An optimal loading amount of 3 mM was then used in subsequent investigations.

The applied voltage is critical for the cycling of $\text{Fe}^{3+}/\text{Fe}^{2+}$ pairs of the Fe–MOF [30]. The TC degradation efficiency was 58.3% ($k = 0.039 \text{ min}^{-1}$), 78.2% ($k = 0.066 \text{ min}^{-1}$) and 98.3% ($k = 0.159 \text{ min}^{-1}$) at applied voltages of -0.5 V , -1.5 V and -2 V , respectively (Figure 4b). The above results indicated that a more negative potential is favorable to boost the TC degradation efficiency [12]. Nevertheless, further decreasing the applied voltage to -2.5 V only led to a decreased TC removal efficiency of 83.3% ($k = 0.082 \text{ min}^{-1}$), possibly due to the occurrence of other side reactions (e.g., hydrogen generation reaction) that decrease the current efficiencies [31].

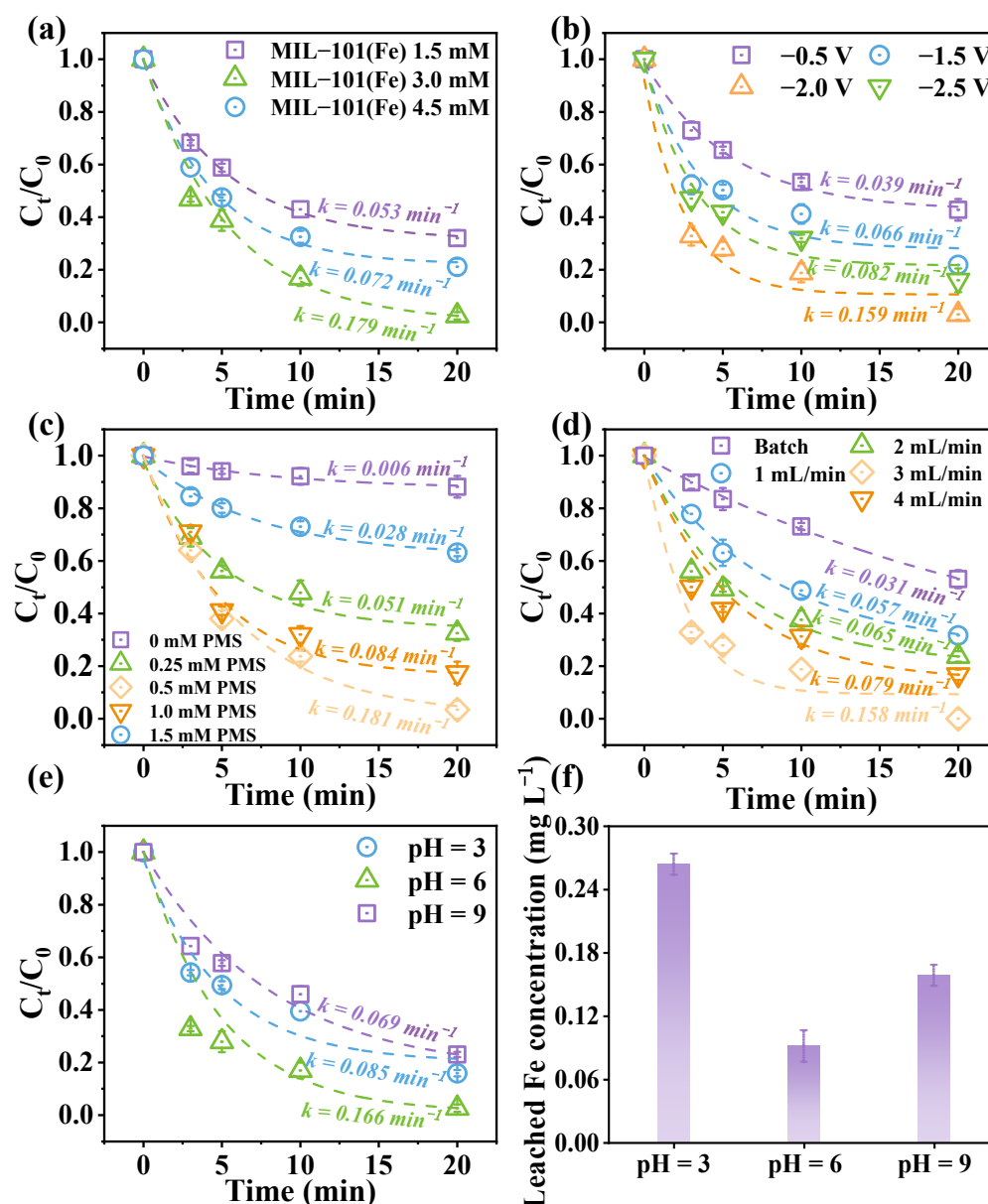


Figure 4. Impact of operational parameters on the TC degradation kinetics: effects of (a) MIL-101(Fe) loading, (b) applied voltage, (c) PMS concentration, (d) flow rate and (e) pH on the TC degradation and (f) concentration of leachable Fe at different pHs. Experimental conditions: MIL-101(Fe)@CNT = 3 mM, $[TC]_0 = 20 \text{ mg L}^{-1}$, applied voltage = -2 V , illumination voltage = 3.8 V , pH = 6.0.

2.4.2. Impacts of PMS Concentration and Flow Rate

In the photoelectrochemical filtration system, PMS acts not only as an electrolyte, but also as a precursor for the reactive species. We, hence, evaluated the effect of PMS dosage on the degradation of TC. As shown in Figure 4c, the TC removal efficiency was only 11.9% in the absence of PMS. The TC removal efficiency (67.5% to 97.1%) and k value (0.028 min^{-1} to 0.181 min^{-1}) were obviously enhanced with increasing PMS concentration from 0.25 to 1.0 mM, which was attributed to more active species being generated. However, further increasing the PMS concentration to 1.5 mM contributed negatively to the TC degradation kinetics (83.1%, $k = 0.084 \text{ min}^{-1}$). This could be associated with active species derived from the catalytic reaction being quenched at higher concentrations of PMS [26].

The effects of flow rate on TC degradation efficiency are shown in Figure 4d. The TC degradation efficiencies were 69.4%, 76.6%, 98.2%, 83.3% and 46.9%, and corresponding k

values were 0.057 min^{-1} , 0.066 min^{-1} , 0.158 min^{-1} , 0.079 min^{-1} and 0.031 min^{-1} at flow rates of 1 mL min^{-1} , 2 mL min^{-1} , 3 mL min^{-1} , 4 mL min^{-1} and batch mode, respectively. Such performance enhancement was attributed to the convection–enhanced mass transport, whereas the batch system relied on diffusion [12]. In addition, the TC degradation efficiency decreased by 14.9% at a higher flow rate in the circulation mode (4 mL min^{-1}), mainly because of the reduced residence time and contact between TC molecules and reactive species at the higher flow rates [13].

2.4.3. Impact of Solution pH

The solution pH poses an effect on the surface charge of the nanohybrid filter as well as the speciation of PMS. As displayed in Figure 4e, the highest removal efficiency of TC (98.8%, $k = 0.166 \text{ min}^{-1}$) was obtained under a neutral pH of 6.0. Under acidic pH conditions, an 85.3% TC can still be obtained since the nanohybrid filter ($\text{pH}_{\text{zpc}} = 3.5$, Figure S7) became positively charged, which attracts the negatively charged HSO_5^- towards the filter surface to complete the catalytic reactions, while the evident performance decay under alkaline condition (77.6%, $k = 0.069 \text{ min}^{-1}$) could be explained by the conversion of HSO_5^- to the weakly reactive SO_5^{2-} and the electrostatic repulsion effect (Equation (12)) [19]. In addition, the leachable Fe during the catalytic reaction was determined as a function of solution pH. As depicted in Figure 4f, the leached iron concentrations were 0.26 mg L^{-1} , 0.09 mg L^{-1} and 0.16 mg L^{-1} at pH values of 3, 6 and 9, respectively. These results indicated that the nanohybrid filter possesses relatively high pH tolerance.



2.5. System Stability Evaluation

Several ubiquitous anions (e.g., Cl^- , NO_3^- , and HCO_3^-) may present in natural waters to negatively impact the system efficacy [32,33]. Thus, the impacts of inorganic constituents on the degradation of TC were investigated. As expected, the presence of Cl^- and NO_3^- posed a negligible influence on the system efficacy with >90% TC degradation (Figure S8a). However, HCO_3^- posed an evident inhibition on the TC degradation efficiency (72.8%) due to its buffering capability to maintain the reaction solution under basic [19]. Moreover, the efficacy of the nanohybrid filter towards the degradation of other refractory organic micropollutants was also evaluated. As displayed in Figure S8b, under similar operation conditions, the photoelectrochemical filtration system still showed excellent degradation performance toward methylene blue (99.8%), Congo red (99.7%) and *p*-nitrophenol (85.6%).

The efficacy of the nanohybrid filter was further examined by spiking TC into tap water, lake water and municipal WWTP effluent, which was considered to be much more complex compared with the ultrapure water used (Figure 5a and Table S6) [12,34].

The results showed that TC degradation efficiencies of 94.3%, 85.9% and 75.6% with corresponding k values of 0.137 min^{-1} , 0.090 min^{-1} and 0.058 min^{-1} , respectively, could be achieved in spiked tap water, lake water and municipal WWTP effluent. Moreover, the stability of the nanohybrid filter was evaluated in consecutive cycles toward TC degradation. The TC degradation efficiencies slightly dropped by 6.1%, 8.9%, 12.2% and 14.2% over five consecutive running cycles, which indicated a decent stability of the system (Figure 5b). These encouraging results indicate that the proposed technology with promising practical application prospects may provide a viable solution for water decontamination.

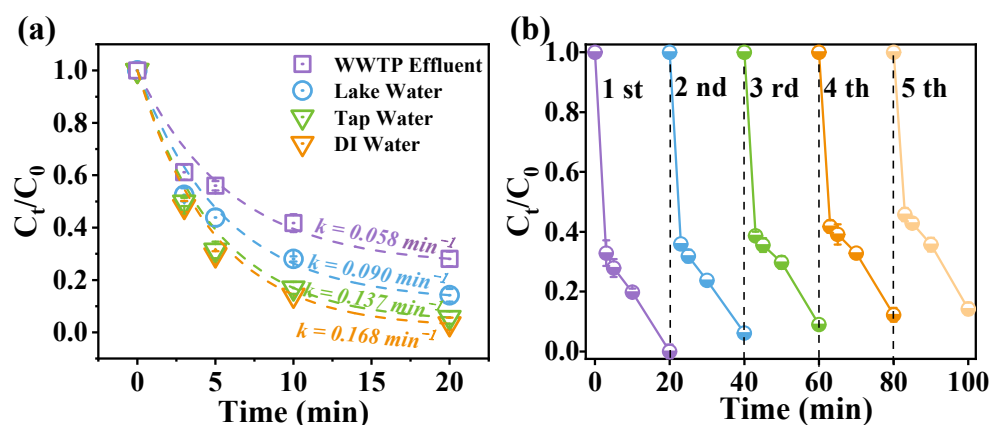


Figure 5. System stability evaluation: (a) The degradation efficiency of TC in different water matrixes. (b) Degradation efficiency of TC in different cycle times. Experimental conditions: MIL-101(Fe)@CNT = 3 mM, $[TC]_0 = 20 \text{ mg L}^{-1}$, applied voltage = -2 V , illumination voltage = 3.8 V , pH = 6.0.

3. Materials and Methods

3.1. Chemicals and Materials

Potassium peroxymonosulfate (PMS, $\text{HKSO}_5 \cdot 0.5\text{HKSO}_4 \cdot 0.5\text{K}_2\text{SO}_4$, $\geq 98.0\%$), dimethylformamide (DMF, $\text{C}_3\text{H}_7\text{NO}$, $\geq 99.5\%$), iron chloride hexahydrate ($\text{FeCl}_3 \cdot 6\text{H}_2\text{O}$, $\geq 99.5\%$), 1,4-benzenedicarboxylic acid (BDC, $\text{C}_8\text{H}_6\text{O}_4$, $\geq 99.9\%$), tetracycline hydrochloride (TC, $\text{C}_{22}\text{H}_{25}\text{ClN}_2\text{O}_8$, $\geq 99.5\%$), Congo red ($\text{C}_{32}\text{H}_{22}\text{N}_6\text{Na}_2\text{O}_6\text{S}_2$, $\geq 98.0\%$), methylene blue ($\text{C}_{16}\text{H}_{18}\text{ClN}_3\text{S}$, $\geq 99.9\%$), *p*-nitrophenol ($\text{C}_6\text{H}_5\text{NO}_3$, $\geq 98.0\%$), ethanol ($\text{C}_2\text{H}_5\text{OH}$, $\geq 96.0\%$), methanol (CH_3OH , $\geq 98.0\%$), hydrochloric acid (HCl, $\geq 36\text{--}38\%$), sodium hydroxide (NaOH, $\geq 96.0\%$), sodium nitrate (NaNO_3 , $\geq 99.9\%$), sodium sulfate (Na_2SO_4 , $\geq 99.0\%$), sodium chloride (NaCl, $\geq 99.5\%$) and sodium bicarbonate (NaHCO_3 , $\geq 99.5\%$) were obtained from Sinopharm Chemical Reagent Co., Ltd. (Shanghai, China). 2,2,6,6-tetramethyl-4-piperidinol (TEMP, $\text{C}_9\text{H}_{20}\text{N}_2$, $\geq 96.0\%$), 5,5-dimethyl-1-pyrroline-*n*-oxide (DMPO, $\text{C}_6\text{H}_{11}\text{NO}$, $\geq 97.0\%$), furfuryl alcohol (FFA, $\text{C}_5\text{H}_6\text{O}_2$, $\geq 98.0\%$), *L*-histidine ($\text{C}_6\text{H}_9\text{N}_3\text{O}_2$, $\geq 99.5\%$), tert-butyl alcohol (TBA, $\text{C}_4\text{H}_{10}\text{O}$, $\geq 98.0\%$) and deuterium oxide (D_2O , $\geq 99.0\%$) were purchased from Sigma-Aldrich (St. Louis, MO, USA). Acidified multi-walled carbon nanotubes (O-CNT) were provided by Times Nano Co., Ltd. (Chengdu, China). All aqueous solutions were prepared by using the ultrapure water produced from a Milli-Q Direct 8 purification system (Millipore, Billerica, MA, USA).

3.2. Synthesis of the Nanohybrid Filter

An MIL-101(Fe)@CNT hybrid filter was synthesized by using a reported solvothermal protocol with modifications [18]. Briefly, in a typical process, 24.3 mg (3 mM) $\text{FeCl}_3 \cdot 6\text{H}_2\text{O}$ and 25 mg CNT were first separately dissolved into 15 mL DMF, followed by sonication for 40 min. Afterwards, 7.5 mg BDC was mixed into 15 mL DMF and then added dropwise into the above solution. The as-obtained mixture was transferred to a 50 mL Teflon-lined autoclave and heated at $110 \text{ }^\circ\text{C}$ for 24 h. The product was loaded onto a polytetrafluoroethylene membrane by vacuum filtration and further purified with DMF and ethanol, and then dried at $60 \text{ }^\circ\text{C}$ under vacuum overnight to obtain the MIL-101(Fe)@CNT nanohybrid filter.

3.3. Characterization

The crystallinity and morphology of the filter samples were characterized, respectively, on a Rigaku D/max-2550 PC thin-film X-ray diffractometer (XRD, Rigaku, Japan) and a field emission scanning electron microscope (FESEM, Hitachi S-4800, Hitachi, Tokyo, Japan). The X-ray photoelectron spectroscopy (XPS) analysis was performed under high vacuum (1×10^{-9} Torr) using a Thermo Fisher Scientific ESCALAB 250Xi (Thermo Fisher Scientific, Waltham, MA, USA) spectrometer. The photochemical and electrochemical activity of the prepared filters were characterized on a CHI660E electrochemical workstation (Shanghai

Chenhua Co., Ltd., Shanghai, China) in a three-electrode system (i.e., MIL-101(Fe)@CNT working anode, Pt counter electrode and Ag/AgCl reference electrode). The preparation of MIL-101(Fe) electrode was referred to in a previous report [11]. Zeta potential was determined on a JS94H micro electrophoresis instrument (Shanghai Zhongchen, China). Reactive species were determined by using a Bruker EMX nano Bench-Top electron paramagnetic resonance (EPR) spectrometer (Bruker, Karlsruhe, Germany).

3.4. TC Degradation Experiments

A commercial filtration casing with photoelectrochemical modifications was employed for organic degradation experiments (Figure S9) [11,13]. All TC degradation experiments were performed after the filter adsorption saturation was reached to eliminate the contribution of physical adsorption. Two operational modes, i.e., recirculated filtration and batch, were conducted for comparison. For the batch mode, the MIL-101(Fe)@CNT nanohybrid filter and titanium sheet were used as a cathode and anode, respectively, and suspended in a beaker containing 50 mL of 20 mg L⁻¹ TC and 1 mM PMS at 2 V. UV LED illumination was introduced by eight NSPU510CS UV LED lamps (NICHIA, Japan) installed on the top of the filtration apparatus. For the recirculation mode, the solution was passed through the filtration system and returned. The PMS concentration (0.25 to 1.5 mM), applied voltage (0.5 to 2 V), MIL-101(Fe) dose (1.5 to 4.5 mM), flow rate (1 to 4 mL min⁻¹) and solution pH (3 to 9) were evaluated and optimized.

The stability of the nanohybrid filter was assessed by performing five consecutive cycles under optimal conditions. A new cycle was initiated after washing the exhausted filter with NaOH solution (5 mM 100 mL) and abundant water solution until the effluent became neutral. The effluent (1 mL) was sampled at predetermined time intervals and immediately mixed with 300 µL methanol to quench any remaining radical species. Subsequently, the TC concentration was quantified by high-performance liquid chromatography (HPLC) [13]. The PMS residual concentration was measured by potassium iodide method [27]. To examine the impact of common coexisting anions on the TC degradation kinetics, 5 mM of nitrate, carbonate or chloride were spiked into TC solution before the recirculated filtration. The practical application potential of the system was verified using the TC-spiked tap water, lake water and municipal wastewater treatment plant (WWTP) effluent as well as an array of other refractory organic contaminants. Detailed characteristics of different water matrices are available in Table S6. The concentration of Congo red, methylene blue and *p*-nitrophenol were determined via a UV-2600 Shimadzu ultraviolet-visible spectrophotometry (Japan) at wavelengths of 497 nm, 665 nm and 317 nm, respectively.

4. Conclusions

In conclusion, we reported and demonstrated a photoelectrochemical filtration system that enables the effective decontamination of antibiotic tetracycline from water. The key to this technology was a nanohybrid filter consisting of electrically conductive CNT and photo-responsive MIL-101(Fe). Various advanced characterizations collectively provided detailed compositional and morphological information on the filter. Results suggested that both radical and nonradical pathways contributed to the effective tetracycline degradation. Moreover, the plug-flow configuration facilitated a convection-enhanced mass transport, further promoting the organic degradation kinetics. Such excellent system efficacy can be maintained across a wide range of solution pH as well as complex water matrices. Overall, the outcomes of this study provide a viable strategy toward water remediation by integrating the state-of-the-art photoelectrochemistry, membrane separation, nanotechnology, and advanced oxidation technologies.

Supplementary Materials: The following are available online at: <https://www.mdpi.com/article/10.3390/catal12040416/s1>. Figure S1: (a) XRD pattern and (b) TGA curves of 3 mM MIL-101(Fe)@CNT and O-CNT; Figure S2: Energy dispersive spectra of the MIL-101(Fe)@CNT filter. Figure S3: (a) Cyclic voltammetry curves of 3 mM MIL-101(Fe)@CNT with or without UV irradiation. (b) Nyquist diagrams of 3 mM MIL-101(Fe)@CNT and MIL-101(Fe). Environmental conditions: $[\text{Na}_2\text{SO}_4]_0 = 50 \text{ mM}$; Figure S4: Residual concentration of PMS in different systems. Experimental conditions: MIL-101(Fe)@CNT = 3 mM, $[\text{TC}]_0 = 20 \text{ mg L}^{-1}$, applied voltage = -2 V , illumination voltage = 3.8 V , pH = 6.0; Figure S5: Effects of (a) adding TBA and (b) reaction solvent (H_2O and D_2O) on the TC degradation. Experimental conditions: MIL-101(Fe)@CNT = 3 mM, $[\text{TC}]_0 = 20 \text{ mg L}^{-1}$, applied voltage = -2 V , illumination voltage = 3.8 V , pH = 6.0; Figure S6: XPS spectra of MIL-101(Fe)@CNT: (a) O 1s and (b) Fe 2p before and after reaction; Figure S7: Zeta spectra of 3 mM MIL-101(Fe)@CNT and O-CNT; Figure S8: (a) Effect of coexisting ions on TC degradation and (b) degradation efficiency of four typical organic compounds by MIL-101(Fe)@CNT filter in circulation mode. Experimental conditions: $[\text{Congo red}]_0 = [\text{Methylene blue}]_0 = 20 \text{ mg L}^{-1}$, $[\text{p-nitrophenol}]_0 = 10 \text{ mg L}^{-1}$, MIL-101(Fe)@CNT = 3 mM, $[\text{TC}]_0 = 20 \text{ mg L}^{-1}$, applied voltage = -2 V , illumination voltage = 3.8 V , pH = 6.0; Figure S9: Schematic illustration of photoelectric reactor device; Table S1: Corresponding k value to TC degradation in different systems according to the pseudo first order kinetic model; Table S2: Corresponding k value to TC degradation in different quenchers according to the pseudo first order kinetic model; Table S3: XPS results of O1s; Table S4: XPS results of Fe 2p; Table S5: Corresponding k value to TC degradation of different operational parameters according to the pseudo first order kinetic model; Table S6: Characteristics of different water samples and corresponding k value to TC degradation.

Author Contributions: W.Z. (Wenchang Zhao) conducted data curation and wrote the original draft. Y.D. performed the experiments. W.Z. (Wentian Zheng) performed formal analysis. Y.L. supervised the study, provided resources, and reviewed and edited the paper. All authors have read and agreed to the published version of the manuscript.

Funding: This work was supported by the Natural Science Foundation of China (No. 52170068).

Data Availability Statement: All relevant data are available from the corresponding author on request.

Conflicts of Interest: The authors declare no conflict of interest.

References

1. Cristian, M.; Antonio, V.; José Luis, V.; Leire, R. Hybrid organic-inorganic membranes for photocatalytic water remediation. *Catalysts* **2022**, *12*, 180. [[CrossRef](#)]
2. Vadivel, D.; Sturini, M.; Speltini, A.; Dondi, D. Tungsten catalysts for visible light driven ofloxacin photocatalytic degradation and hydrogen production. *Catalysts* **2022**, *12*, 310. [[CrossRef](#)]
3. Azar, F.; Ivana, J.; Nivetha, S.; Leslie, B.; Robert, L.; Norman, Z.; Mark, S.; Maricor, A. Effect of background water matrices on pharmaceutical and personal care product removal by UV-LED/TiO₂. *Catalysts* **2021**, *11*, 576. [[CrossRef](#)]
4. Xu, Y.; Yu, X.; Xu, B.; Peng, D.; Guo, X. Sorption of pharmaceuticals and personal care products on soil and soil components: Influencing factors and mechanisms. *Sci. Total Environ.* **2020**, *753*, 141891. [[CrossRef](#)] [[PubMed](#)]
5. Zhang, C.; Chen, X.; Ho, S. Wastewater treatment nexus: Carbon nanomaterials towards potential aquatic ecotoxicity. *J. Hazard. Mater.* **2021**, *417*, 125959. [[CrossRef](#)] [[PubMed](#)]
6. Zheng, W.T.; Liu, Y.B.; Liu, W.; Ji, H.D.; Li, F.; Shen, C.S.; Fang, X.F.; Li, X.; Duan, X.G. A novel electrocatalytic filtration system with carbon nanotube supported nanoscale zerovalent copper toward ultrafast oxidation of organic pollutants. *Water Res.* **2021**, *194*, 116961. [[CrossRef](#)] [[PubMed](#)]
7. Zhou, C.; Zhu, L.; Deng, L.; Zhang, H.; Zeng, H.; Shi, Z. Efficient activation of peroxymonosulfate on CuS@MIL-101(Fe) spheres featured with abundant sulfur vacancies for coumarin degradation: Performance and mechanisms. *Sep. Purif. Technol.* **2021**, *276*, 119404. [[CrossRef](#)]
8. Wu, D.; Xia, K.; Fang, C.; Chen, X.; Ye, Y. Rapid removal of azophloxine via catalytic degradation by a novel heterogeneous catalyst under visible light. *Catalysts* **2020**, *10*, 138. [[CrossRef](#)]
9. Liu, Y.B.; Liu, F.Q.; Ding, N.; Hu, X.H.; Shen, C.S.; Li, F.; Huang, M.H.; Wang, Z.W.; Sand, W.; Wang, C.C. Recent advances on electroactive CNT-based membranes for environmental applications: The perfect match of electrochemistry and membrane separation. *Chin. Chem. Lett.* **2020**, *31*, 2539–2548. [[CrossRef](#)]
10. Ren, Y.L.; Liu, Y.B.; Liu, F.Q.; Li, F.; Shen, C.S.; Wu, Z.C. Extremely efficient electro-Fenton-like Sb(III) detoxification using nanoscale Ti-Ce binary oxide: An effective design to boost catalytic activity via non-radical pathway. *Chin. Chem. Lett.* **2021**, *32*, 2519–2523. [[CrossRef](#)]

11. Li, M.H.; Liu, Y.B.; Shen, C.S.; Li, F.; Wang, C.C.; Huang, M.H.; Yang, B.; Wang, Z.W.; Yang, J.M.; Sand, W. One-step Sb(III) decontamination using a bifunctional photoelectrochemical filter. *J. Hazard. Mater.* **2020**, *389*, 121840. [[CrossRef](#)] [[PubMed](#)]
12. Liu, Y.B.; Gao, G.D.; Vecitis, C.D. Prospects of an electroactive carbon nanotube membrane toward environmental applications. *Acc. Chem. Res.* **2020**, *53*, 2892–2902. [[CrossRef](#)] [[PubMed](#)]
13. Guo, D.L.; Liu, Y.B.; Ji, H.D.; Wang, C.C.; Chen, B.; Shen, C.S.; Li, F.; Wang, Y.X.; Lu, P.; Liu, W. Silicate-enhanced heterogeneous flow-through electro-Fenton system using iron oxides under nanoconfinement. *Environ. Sci. Technol.* **2021**, *55*, 4045–4053. [[CrossRef](#)] [[PubMed](#)]
14. Debashis, R.; Sudarsan, N.; Sirshendu, D. Mechanistic investigation of photocatalytic degradation of Bisphenol-A using MIL-88A(Fe)/MoS₂ Z-scheme heterojunction composite assisted peroxymonosulfate activation. *Chem. Eng. J.* **2021**, *428*, 131028. [[CrossRef](#)]
15. Zhang, S.; Zhao, Y.; Yang, K.; Liu, W.; Xu, Y.; Liang, P.; Zhang, X.; Huang, X. Versatile zero valent iron applied in anaerobic membrane reactor for treating municipal wastewater: Performances and mechanisms. *Chem. Eng. J.* **2020**, *382*, 123000. [[CrossRef](#)]
16. Liu, B.; Song, W.; Wu, H.; Liu, Z.; Teng, Y.; Sun, Y.; Xu, Y.; Zheng, H. Degradation of norfloxacin with peroxymonosulfate activated by nanoconfinement Co₃O₄@CNT nanocomposite. *Chem. Eng. J.* **2020**, *398*, 125498. [[CrossRef](#)]
17. Guo, D.L.; You, S.J.; Li, F.; Liu, Y.B. Engineering carbon nanocatalysts towards efficient degradation of emerging organic contaminants via persulfate activation: A review. *Chin. Chem. Lett.* **2022**, *33*, 1–10. [[CrossRef](#)]
18. Xiao, Z.; Feng, X.; Shi, H.; Zhou, B.; Wang, W.; Ren, N. Why the cooperation of radical and non-radical pathways in PMS system leads to a higher efficiency than a single pathway in tetracycline degradation. *J. Hazard. Mater.* **2021**, *424*, 127247. [[CrossRef](#)]
19. Jin, L.M.; You, S.J.; Duan, X.G.; Yao, Y.; Yang, J.M.; Liu, Y.B. Peroxymonosulfate activation by Fe₃O₄-MnO₂/CNT nanohybrid electroactive filter towards ultrafast micropollutants decontamination: Performance and mechanism. *J. Hazard. Mater.* **2022**, *423*, 127111. [[CrossRef](#)]
20. Wang, C.; Du, J.; Liang, Z.; Liang, J.; Zhao, Z.; Cui, F.; Shi, W. High efficiency oxidation of fluoroquinolones by the synergistic activation of peroxymonosulfate via vacuum ultraviolet and ferrous iron. *J. Hazard. Mater.* **2021**, *422*, 126884. [[CrossRef](#)]
21. Li, N.; Tang, S.; Rao, Y.; Qi, J.; Zhang, Q.; Yuan, D. Peroxymonosulfate enhanced antibiotic removal and synchronous electricity generation in a photocatalytic fuel cell. *Electrochim. Acta* **2018**, *298*, 56–69. [[CrossRef](#)]
22. Xie, X.; Cao, J.; Xiang, Y.; Xie, R.; Suo, Z.; Ao, Z.; Yang, X.; Huang, H. Accelerated iron cycle inducing molecular oxygen activation for deep oxidation of aromatic VOCs in MoS₂ co-catalytic Fe³⁺/PMS system. *Appl. Catal. B Environ.* **2022**, *309*, 121235. [[CrossRef](#)]
23. Yang, Q.; Yan, Y.; Yang, X.; Liao, G.; He, J.; Wang, D. The effect of complexation with metal ions on tetracycline degradation by Fe²⁺/Fe³⁺ and Ru³⁺ activated peroxymonosulfate. *Chem. Eng. J.* **2021**, *429*, 132178. [[CrossRef](#)]
24. Jiang, Y.; Wang, Z.; Huang, J.; Yan, F.; Du, Y.; He, C.; Liu, Y.; Yao, G.; Lai, B. A singlet oxygen dominated process through photocatalysis of CuS-modified MIL-101(Fe) assisted by peroxymonosulfate for efficient water disinfection. *Chem. Eng. J.* **2022**, *439*, 135788. [[CrossRef](#)]
25. Bi, H.; Liu, C.; Li, J.; Tan, J. Insights into the visible-light-driving MIL-101 (Fe)/g-C₃N₄ materials-activated persulfate system for efficient hydrochloride water purification. *J. Solid State Chem.* **2022**, *306*, 122741. [[CrossRef](#)]
26. Zheng, W.T.; You, S.J.; Yao, Y.; Jin, L.M.; Liu, Y.B. Development of atomic hydrogen-mediated electrocatalytic filtration system for peroxymonosulfate activation towards ultrafast degradation of emerging organic contaminants. *Appl. Catal. B Environ.* **2021**, *298*, 120593. [[CrossRef](#)]
27. Zuo, S.; Xia, D.; Guan, Z.; Yang, F.; Zhang, B.; Xu, H.; Huang, M.; Guo, X.; Li, D. The polarized electric field on Fe₂O₃/g-C₃N₄ for efficient peroxymonosulfate activation: A synergy of ¹O₂, electron transfer and pollutant oxidation. *Sep. Purif. Technol.* **2021**, *269*, 118717. [[CrossRef](#)]
28. Li, J.; Liu, Q.; Gou, G.; Kang, S.; Tan, X.; Tan, B.; Li, L.; Li, N.; Liu, C.; Lai, B. New insight into the mechanism of peroxymonosulfate activation by Fe₃S₄: Radical and non-radical oxidation. *Sep. Purif. Technol.* **2022**, *286*, 120471. [[CrossRef](#)]
29. Cheng, X.; Guo, H.G.; Zhang, Y.L.; Wu, X.; Liu, Y. Non-photochemical production of singlet oxygen via activation of persulfate by carbon nanotubes. *Water Res.* **2017**, *113*, 80–88. [[CrossRef](#)]
30. Zhang, Y.; Chu, W. G-C₃N₄ induced acceleration of Fe³⁺/Fe²⁺ cycles for enhancing metronidazole degradation in Fe³⁺/peroxymonosulfate process under visible light. *Chemosphere* **2022**, *293*, 133611. [[CrossRef](#)]
31. Dai, Y.L.; Yao, Y.; Li, M.H.; Fang, X.F.; Shen, C.S.; Li, F.; Liu, Y.B. Carbon nanotube filter functionalized with MIL-101(Fe) for enhanced flow-through electro-Fenton. *Environ. Res.* **2022**, *204*, 112117. [[CrossRef](#)] [[PubMed](#)]
32. Chen, X.; Han, Y.; Gao, P.; Li, H. New insight into the mechanism of electro-assisted pyrite minerals activation of peroxymonosulfate: Synergistic effects, activation sites and electron transfer. *Sep. Purif. Technol.* **2021**, *274*, 118817. [[CrossRef](#)]
33. Wang, W.; Wu, Q.; Huang, N.; Wang, T.; Hu, H. Synergistic effect between UV and chlorine (UV/chlorine) on the degradation of carbamazepine: Influence factors and radical species. *Water Res.* **2016**, *98*, 190–198. [[CrossRef](#)] [[PubMed](#)]
34. Zhong, S.; Yang, B.; Xiong, Q.; Cai, W.; Lan, Z.; Ying, G. Hydrolytic transformation mechanism of tetracycline antibiotics: Reaction kinetics, products identification and determination in WWTPs. *Ecotoxicol. Environ. Saf.* **2021**, *229*, 113063. [[CrossRef](#)] [[PubMed](#)]